

# Automated generation of photonic circuits for Bell tests with homodyne measurements

Corentin Lanore<sup>1</sup>, Federico Grasselli<sup>1,2</sup>, Xavier Valcarce<sup>1</sup>, Jean-Daniel Bancal<sup>1</sup>, and Nicolas Sangouard<sup>1</sup>

<sup>1</sup>Université Paris-Saclay, CEA, CNRS, Institut de physique théorique, 91191, Gif-sur-Yvette, France

<sup>2</sup>Leonardo Innovation Labs – Quantum Technologies, Via Tiburtina km 12,400, 00131 Rome, Italy

**Nonlocal quantum realizations, certified by the violation of a Bell inequality, are core resources for device-independent quantum information processing. Although proof-of-principle experiments demonstrating device-independent quantum information processing have already been reported, identifying physical platforms that are realistically closer to practical, viable devices remains a significant challenge. In this work, we present an automated framework for designing photonic implementations of nonlocal realizations using homodyne detections and quantum state heralding. Combining deep reinforcement learning and efficient simulations of quantum optical processes, our method generates photonic circuits that achieve significant violations of the Clauser-Horne-Shimony-Holt inequality. In particular, we find an experimental setup, robust to losses, that yields a CHSH violation of 2.068 with 3.9 dB and 0.008 dB squeezed light sources and two beam splitters.**

## 1 Introduction

As demonstrated by the violation of Bell inequalities, quantum mechanics allows for entangled particles to exhibit nonlocal correlations that cannot be explained by any local hidden variable model [1, 2]. Initially studied to probe the foundations of quantum theory, nonlocality has now found applications in the device-independent (DI) processing of quantum information [3, 4]. Most notably, nonlocality enables the certifica-

tion of quantum resources via self-testing [5, 6] and it is necessary to derive device-independent security proofs for quantum key distribution [7–13] and to demonstrate the device-independent generation of quantum random numbers [14].

The nonlocality certified by a violation of the Clauser-Horne-Shimony-Holt (CHSH) inequality [15], a bipartite Bell inequality, stands at the core of numerous DI protocols. Loophole-free violations of the CHSH inequality have been accomplished using a variety of platforms, from NV-centers [16] and photonic setup [17–21] to neutral atoms [22] and superconducting circuits [23]. Efforts aiming to generate high CHSH violations at high rates have culminated with the first distribution of a device-independent key using trapped ions [24]. Results have also been obtained to extend DIQKD over hundreds of meters with single atoms [25]. On-going efforts [26] aims at implementing device-independent quantum information processing with a purely photonic platform – a platform where optical modes are entangled, manipulated and detected – which is plausibly closer to what is expected for a commercial device.

With their high efficiency, low noise, high bandwidth and capability to operate at telecom wavelengths at room temperature, homodyne detectors are a natural candidate for implementing practical Bell tests. Coupled with a fully photonic circuit for state generation and manipulation, Bell tests may be implemented using integrated on-chip devices. Encouragingly, it has been shown that high CHSH violations can be achieved with homodyne measurements [27–30]. However, these proposals require tailored states whose experimental realizations is either unknown or, in the best of cases, very challenging. Meanwhile, realistic optical setups with

Xavier Valcarce: [xavier.valcarce@ipht.fr](mailto:xavier.valcarce@ipht.fr)

homodyne detectors achieving a CHSH score of  $\mathcal{B} \approx 2.048$  have been proposed [31, 32]. This score is, however, below the threshold required by some DI protocols [33, 34]. Therefore, designing realistic optical setups with homodyne detection leading to higher CHSH scores remains an open problem.

With advances in integrated photonic circuits [35, 36], the implementation of circuits with a high number of elements and modes becomes possible, thus increasing the set of accessible optical states for CHSH tests. It is however challenging to discover suitable optical circuits, as the number of possible circuits grows exponentially with the number of optical elements considered.

In this work, we tackle circuit discovery with an automated approach that combines machine learning with an efficient simulation of optical circuits based on Gaussian representation of quantum states. Specifically, we use deep reinforcement learning for the design of practical photonic CHSH tests, characterized by standard optical components and homodyne measurements. Deep reinforcement learning has proven to be highly effective in discovering relevant elements in a large exploration space [37–41] and has already been applied to many quantum physics tasks [42–45], including optical circuits design [46–49].

Our approach allows for the exploration of photonic circuits in different configurations by enforcing constraints on, e.g., the number of optical modes or the set of available optical elements. This can narrow the search to specific sets of photonic circuits that reflect experimental constraints or leverage knowledge on photonic systems. We find numerous optical circuits yielding significant CHSH scores up to  $\mathcal{B} \approx 2.076$ . In particular, we propose a simple setup composed of four bosonic modes and four optical components that produces a CHSH score of  $\mathcal{B} \approx 2.068$ . This setup yields CHSH violations for parties separated by more than 8 kilometers, while requiring at most 3.9 dB of squeezed light. We believe this proposed setup could lead to a first Bell test with homodyne measurements and pave the way for more practical implementations of DI protocols.

## 2 Preliminaries

### 2.1 The CHSH Inequality

Bell tests allow detecting nonlocal quantum correlations by ruling out local hidden variable models for these correlations. In this manuscript, we consider a Bell test involving two parties, Alice and Bob, and subdivided into rounds. In each round, Alice picks a measurement setting by selecting one of two inputs  $x \in \{0, 1\}$ , and collects the measurement outcome  $a \in \{1, -1\}$ . Similarly, Bob chooses a setting  $y \in \{0, 1\}$  and obtains an outcome  $b \in \{1, -1\}$ . With sufficiently many rounds, the parties can estimate the correlators

$$\langle A_x B_y \rangle = P(a = b|x, y) - P(a \neq b|x, y), \quad (1)$$

where  $P(a = b|x, y)$  (resp.  $P(a \neq b|x, y)$ ) is the probability that the outcomes  $a$  and  $b$  are equal (differ), given inputs  $x$  for Alice and  $y$  for Bob.

In the case where the outcome correlations are compatible with a local hidden variable model, the Clauser-Horne-Shimony-Holt score

$$\mathcal{B} = |\langle A_0 B_0 \rangle + \langle A_0 B_1 \rangle + \langle A_1 B_0 \rangle - \langle A_1 B_1 \rangle| \quad (2)$$

satisfies the CHSH inequality [15]

$$\mathcal{B} \leq 2. \quad (3)$$

Interestingly, quantum mechanics allows for violations of the CHSH inequality. This can be achieved using incompatible measurements on a shared entangled state [2]. In particular, by performing appropriate projective measurements on two-qubit maximally entangled states, the CHSH score can reach the maximum quantum value of  $\mathcal{B} = 2\sqrt{2}$ , known as the Tsirelson bound [50].

### 2.2 Photonic Circuits

As we focus on practical photonic implementations of Bell tests, we first revisit the relevant concepts of quantum optics. After a brief introduction to photonics, we present Gaussian states and operations that can be accessed using standard optical components. We then review homodyne measurements and the binning of their outcomes, which are used to compute the CHSH score. Finally, we highlight the heralding of quantum states based on detection events with threshold detectors. Further details are reported in Appendix A.

**Photonics** The quadrature field operators of a bosonic mode are expressed in terms of ladder operators using  $\hat{x} = (\hat{a}^\dagger + \hat{a})/2$  and  $\hat{p} = i(\hat{a}^\dagger - \hat{a})/2$ , such that  $[\hat{x}, \hat{p}] = i/2$  holds. Given  $N$  bosonic modes, we arrange these operators in a vector  $\hat{\mathbf{q}} = (\hat{x}_1, \hat{p}_1, \dots, \hat{x}_n, \hat{p}_n)$ .

**Gaussian states** Let  $\hat{\rho}$  be an  $N$ -mode bosonic state. We define its displacement vector  $\boldsymbol{\mu}$  to be composed of elements  $\mu_i = \text{tr}[\hat{q}_i \hat{\rho}]$ , and its covariance matrix  $\Sigma$  to have elements  $\Sigma_{i,j} = \text{tr}[(\hat{q}_i \hat{q}_j + \hat{q}_j \hat{q}_i) \hat{\rho}]/2 - \mu_i \mu_j$ . Gaussian states are a class of quantum states which are completely characterized by their displacement vector and covariance matrix.

**Gaussian operations** Unitary transformations that map Gaussian states into other Gaussian states are called Gaussian operations or Gaussian gates. These operations can be described directly in terms of their action on the displacement vector and the covariance matrix

$$\boldsymbol{\mu} \mapsto M\boldsymbol{\mu} + \mathbf{d} \quad (4)$$

$$\Sigma \mapsto M\Sigma M^\dagger, \quad (5)$$

where  $M$  is a symplectic matrix. In this manuscript we consider four types of gates: two passive operations, beam splitters,  $\hat{B}(\theta)$  and phase shifters  $\hat{R}(\theta)$ , as well as two active ones, namely single-mode and two-mode squeezers, labeled  $\hat{S}_1(r)$  and  $\hat{S}_2(r)$  respectively. Note that these operations are all characterized by  $\mathbf{d} = \vec{0}$ , therefore leaving the displacement vector invariant if applied to a state with  $\boldsymbol{\mu} = \vec{0}$ . The exact expressions of these transformations are reported in Table 1 of Appendix A.2.

**Homodyne measurements** Homodyne measurements are measurements of quadratures of the bosonic field. In the Bell scenario we consider, Alice and Bob measure the quadratures of bosonic mode 1 and 2, respectively, with a randomly chosen measurement setting  $x$  and  $y$ . Each setting corresponds to the measurement of a (fixed) rotated quadrature

$$\hat{x}_1^{\theta_x} = \cos(\theta_x)\hat{x}_1 + \sin(\theta_x)\hat{p}_1, \quad (6)$$

$$\hat{x}_2^{\phi_y} = \cos(\phi_y)\hat{x}_2 + \sin(\phi_y)\hat{p}_2. \quad (7)$$

Such measurements can be implemented by a measurement of the  $\hat{x}_i$  quadrature, preceded by a phase shifter with phase  $\theta_x$  or  $\phi_y$ , accordingly. The joint probability distribution over the continuous spectra of the two parties' measured quadratures is given by

$$P(x_1^{\theta_x}, x_2^{\phi_y}) = \iint_{-\infty}^{\infty} dp_1 dp_2 \tilde{W}_{12}^{xy}(x_1, p_1, x_2, p_2) \quad (8)$$

where  $\tilde{W}_{12}^{xy}$  is the Wigner function of the two-mode bosonic state shared by Alice and Bob, after local phase shifts with angle  $\theta_x$  on Alice's mode and angle  $\phi_y$  on Bob's mode.

As the CHSH scenario requires binary outcomes, we bin the continuous spectra using sign binning. This leads to the expression

$$\langle A_x B_y \rangle = \iint_{-\infty}^{\infty} \text{sign}(x_1^{\theta_x} x_2^{\phi_y}) P(x_1^{\theta_x}, x_2^{\phi_y}) dx_1^{\theta_x} dx_2^{\phi_y} \quad (9)$$

for the correlators defined in Eq. (1). In Appendix A.4, we detail how we numerically compute the above expression.

**Heralding quantum states** Gaussian states and homodyne measurements alone are not suited for Bell inequality violations. Indeed, the statistics generated by Gaussian states and homodyne measurements always admit a local hidden variable model [51, 52], as the Wigner functions of both the state and the observables are non-negative. Conversely, non-Gaussian measurements such as photon-counting devices are described by Wigner functions that can be negative, thereby allowing for Bell violations with Gaussian states [53]. In this work we take the opposite avenue to Bell violations, i.e. we perform homodyne measurements on states with negative Wigner functions.

To obtain states with negative Wigner functions, we herald Gaussian states using threshold detectors. In particular, a heralded two-mode state  $\rho_{12}$  can be obtained from an  $N$ -mode Gaussian state by measuring the presence of one (or more) photons in the other  $N-2$  modes [54]. The resulting state can be written as a linear combination of Gaussian states

$$\hat{\rho}_{12} = \sum_{k=1}^{2^{N-2}} \omega_k \hat{\rho}_{12}^k, \quad (10)$$

with coefficients  $\omega_k \in \mathbb{R}$  satisfying <sup>1</sup>  $\sum_k \omega_k = 1$ , and where  $\hat{\rho}_{12}^k$  are normalized two-mode Gaussian states. Since the Wigner function is linear in the density operator, the Wigner function of such heralded state may become negative in part of the phase space when some of the coefficients  $\omega_k$  are negative. Further details on the expression of heralded states and their creation with threshold detectors are given in Appendix A.3.

### 2.3 Deep Reinforcement Learning

Reinforcement learning (RL) is one of the three paradigms of machine learning. It is characterized by a trial-and-error approach to problem solving, which does not require pre-existing data for the training process. Instead, RL relies on an agent interacting with an environment and receiving feedback in the form of rewards, which are based on the impact of the agent’s actions. Through these interactions, the agent learns a policy, i.e. a probabilistic strategy which aims at maximizing the cumulative reward over time.

The RL training process consists of a sequence of episodes, where each episode is composed of a series of steps. At each step, the agent observes the current state of the environment,  $s$ , and selects an action,  $a$ , by sampling from the policy  $\pi(a|s)$  – the probability to take action  $a$  given a state  $s$ . The action is executed on the environment and a reward  $r$  is returned to the agent. When a given termination condition is met, e.g. a maximum number of steps, the episode stops and the environment is reset to its initial state. After a given number of episodes, the policy is optimized by learning from the past interactions with the environment (the sets of states, actions and respective rewards) with the aim of maximizing the cumulative rewards.

Policy optimization in RL can be tackled by a variety of algorithms. In this work we focus on the proximal policy optimization (PPO), introduced in [41], which balances exploration and exploitation while maintaining a stable and sample-efficient training. In the PPO algorithm, the policy is optimized by iteratively updating it using a clipped surrogate objective function, which prevents drastic updates hence ensuring stability.

<sup>1</sup>Note that the coefficients  $\omega_k$  need to satisfy additional constraints in order to ensure the positivity of the state  $\hat{\rho}_{12}$ .

More specifically, PPO uses two neural networks: the policy network, which outputs a probability distribution  $\pi(a|s)$  over actions  $a$  conditioned on a state  $s$ , and the value network, which returns an estimation  $V(s)$  of the expected cumulative reward from a state  $s$ . Both networks take as input the current state of the environment  $s$ . At each policy update, the weights of the policy network and the value network are updated to match the learned optimal policy and the received cumulative reward, respectively.

## 3 Automated generation of photonic Bell tests

We employ RL, in combination with efficient circuit simulation and numerical optimization, to automate the generation of practical photonic circuits yielding CHSH violations.

### 3.1 Photonic Bell tests as a learning task

In the following, we formulate the tasks of finding photonic Bell tests in the *agent-environment* framework of reinforcement learning. More specifically, we present the environment implementations and the set of actions the agent can interact with, the state and reward received as feedback, as well as an episode routine from initial conditions to termination.

The environment is chosen to be an  $N$ -mode optical circuit, where the first mode is sent to Alice while Bob receives the second one. As an initial condition, each mode is set to the vacuum state. The agent acts on the environment by appending photonic gates to the optical circuit. Each action is identified by the selected gate, either a beam splitter  $\hat{B}(\theta)$ , phase shifter  $\hat{R}(\theta)$ , single-mode squeezer  $\hat{S}_1(r)$  or two-mode squeezer  $\hat{S}_2(r)$ , and the mode or modes on which the gate is applied. At this stage, the parameters of each photonic gate are fixed to a predefined value in order to limit the size of the action space during training. After each action on the environment, the agent receives in return a state and a reward. Finally, once the circuit depth (i.e. number of gates) reaches a maximum predefined value  $n_{\text{circuit}}$ , we terminate the episode and reset the photonic circuit to empty modes.

The state returned by the environment is given by the photonic state shared between Alice and

Bob. This state is computed by applying the current gates in the circuit and by heralding the state of the first two modes on a photon detection in each of the last  $N - 2$  modes. This computation is efficiently carried out numerically by the code which is made available in Ref. [55]. As the heralded state can be seen as a linear combination of  $2^{N-2}$  Gaussian states, as in Eq. (10), we represent it as a vector of  $2^{N-2}(10+1)$  real elements. More specifically, the vector is a concatenation over all  $k$  of the 10 elements of the covariance matrix of each Gaussian state, c.f. Appendix A.1,  $\hat{\rho}_{12}^k$ , followed by the coefficients  $\omega_k$  of the linear combination (remember that the Gaussian parameter  $\mu$  is always zero here so we do not need to store it). Note that if the photon detection probability in one of the heralded modes is below a certain threshold, set to  $10^{-10}$ , the heralding is considered failed to avoid numerical errors (note that this still allows for a global heralding probability smaller than  $10^{-10}$  in the presence of several heralding modes). In this case, the state passed to the agent is a trivial two-mode vacuum state.

As the cumulative reward over the course of an episode is the quantity the policy aims at maximizing, we give a reward of zero for all but the last step. For the last step, i.e. once the circuit is composed of  $n_{\text{circuit}}$  gates, we compute the CHSH score of the total circuit by maximizing  $\mathcal{B}$  over all the optical gates' parameters with the measurement setting  $\{\theta_0, \theta_1\} = \{0, \pi/2\}$  and  $\{\phi_0, \phi_1\} = \{-\pi/4, \pi/4\}$ , and using sign binning. This is done using the Nelder-Mead algorithm. The reward received by the agent is an increasing function of the CHSH score

$$r(\mathcal{B}) = \begin{cases} \frac{\mathcal{B}}{4} - 1 & \text{if } \mathcal{B} < 2 \\ \exp[10 \ln(2)(\mathcal{B} - 2)] - 1 & \text{otherwise.} \end{cases} \quad (11)$$

This expression of the reward has been crafted empirically to favour high CHSH score, even when small improvements are observed.

### 3.2 Learning to design Bell tests

A PPO agent is entrusted with learning to design practical photonic Bell tests. This makes use of a two-headed four-layer neural network, for the policy and value network. The input layer encodes the parameters of the heralded state while the neurons of the output layer represent different actions for the policy head, and the single neuron of

the value-head returns the scalar  $V(s)$ . The number of neurons in the two hidden layers is chosen depending on the size of the state parametrization and the size of the action space. For example, we choose 150 and 90 neurons in the first and second hidden layer, respectively, when testing circuits with  $N = 6$  modes where we restrict the agent's actions to only passive gates. We instead choose 45 and 30 neurons for  $N = 4$  modes and arbitrary gates. We use the PPO agent implementation of the Julia Reinforcement Learning package [56], and rely on the default hyperparameters except for the update frequency and the trajectory capacity, which are set to 64 and 256, respectively.

### 3.3 Exploration and learning strategies

In order to maximize the efficiency of the learning process, we refine our circuit construction model within the framework defined above by identifying several learning strategies. These strategies are motivated by physical and machine learning insights as well as initial benchmarks, and amount to choices of circuit initialization and restrictions on the sets of gates available to the RL agent. An initial study of these strategies by random search allows us to launch the RL algorithm only on the most suitable strategies. Additionally, we consider several heralding schemes as detailed below.

The first circuit-building strategy we consider is the most general one in which the circuit is initialized in the vacuum state and the agent is allowed to pick any of the four gates ( $\hat{B}(\theta)$ ,  $\hat{R}(\theta)$ ,  $\hat{S}_1(r)$  and  $\hat{S}_2(r)$ ) in every interaction with the environment. This strategy has the merit of letting the agent free to choose the optimal circuit configuration, but it comes at the cost of a large action space. Moreover, this strategy permits circuit configurations where multiple squeezers act on the same mode yielding large squeezing parameters. Actually, the agent is probably incentivized to abuse of squeezers as they can increase the amount of entanglement and enhance the CHSH violations. However, the use of sequential squeezing may be hard to achieve experimentally, and it can easily cause numerical errors that lead to unrealistic CHSH scores. Another shortcoming of this strategy is that the agent will inevitably attempt to place passive gates at the beginning of the circuit during training, which would have no effect since they act on the vacuum, thereby de-

creasing the circuit depth available to the agent. For these reasons, we define additional strategies which avoid these limitations.

Concretely, we consider four supplementary strategies in which the circuit is initialized with some fixed active gates that generate photons (single- or two-mode squeezers) and the agent is only allowed to choose gates that are passive (phase shifter and beam splitter) for the rest of the episode. The specific initialization of each strategy is described in Appendix B. These new strategies avoid the unnecessary action choices present in the first strategy because the circuit is initialized in a state containing photons in each mode. Additionally, the risk of too large squeezing parameters is reduced by the presence of at most one squeezer per mode. This constraint also favors experimentally realistic setups as chaining squeezing operations appears challenging. It should be noted that despite limiting the agent to passive gates only, these strategies are not restrictive. Indeed, the Euler decomposition (c.f. Appendix A) guarantees that an arbitrary circuit initialized in the vacuum can always be reproduced by a circuit initialized with squeezers and completed by only passive gates. Finally, by reducing the size of the action space, such strategies can favour the learning process of the agent.

In order to identify the most suitable of these exploration strategies, we test them on random circuits. Namely, we construct circuits by appending successively uniformly chosen random gates from the chosen set until the circuit depth  $n_{\text{circuit}}$  is reached. With no reliance on neural networks, such a random search is light on computational resource and, therefore, allows for the automated exploration of many more circuits in a given time. In particular, a random exploration may provide a circuit yielding a suitable CHSH score. This exploration is however unstructured and less scalable. In our case, we use the result of this investigation to identify the most suitable exploration strategies for reinforcement learning (see Appendix B for more details).

Further preliminary tests also show that circuits with  $N = 3$  and  $N = 5$  modes return weak results. We thus focus our automated search on circuits with  $N = 4$  and  $N = 6$  modes.

Finally, for each considered circuit building strategy, we consider two heralding mechanisms for the last  $N - 2$  modes. In the first scheme,

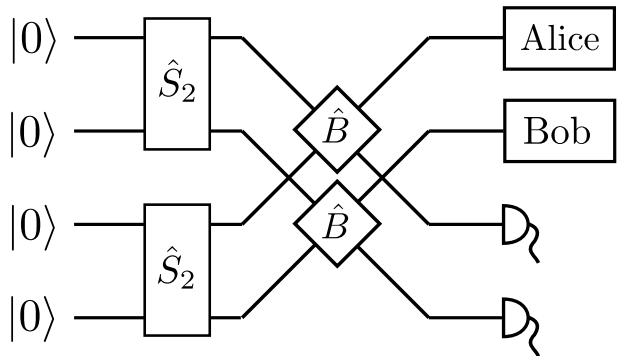


Figure 1: Optical circuit resulting from our automated search. The circuit is composed of two two-mode squeezers ( $\hat{S}_2$ ) acting on modes (1, 2) and (3, 4) with respective parameters  $r = 0.00096$  and  $r = 0.44993$ , followed by two beam splitters ( $\hat{B}$ ) on modes (1, 3) and (2, 4), with respective parameters  $\theta = 1.50272$  and  $\theta = 1.63856$ . The state of modes (1, 2), shared by Alice and Bob, is heralded on a click in both the threshold detectors of modes (3, 4). Alice and Bob measure their modes with homodyne measurements and can obtain an average CHSH score of  $\mathcal{B} = 2.068$ .

we select states based on detection events from threshold detectors applied to each of the last  $N - 2$  modes. A threshold detector differentiates between vacuum and the presence of one or more photons. In the second heralding scheme, we aim to better approximate the single-photon subtraction operation, which is known to introduce non-Gaussianity that is essential for generating nonlocality [54]. This is achieved using an unbalanced beam splitter with high transmittivity, along with a threshold detector at each output port. We select events where a click occurs in the reflected port and a vacuum is detected in the transmitted port. For further details on both heralding schemes, we refer the reader to Appendix B.

## 4 Results

In this section we discuss the optical circuits for CHSH violation obtained with our automated approach. We then focus on a specific circuit, depicted in Fig. 1, which has the merit of being relatively simple while providing a significant CHSH score. We analyse the resilience of this circuit to photon loss with distance between the parties, as well as its compatibility with inefficient detectors.

Using the selected strategies, the PPO agent produced several optical circuits admitting a sig-

nificant violation of the CHSH inequality. In particular, when acting on  $N = 4$  modes, the agent found a circuit producing the score  $\mathcal{B} = 2.069$ , a slightly larger value than the best score  $\mathcal{B} = 2.068$  obtained when using random search in this setting.

However, we also observe that in a given allocated time, the agent could not consistently outperform the random search. In presence of  $N = 6$  modes, for instance, the best circuit identified by the PPO approach reached  $\mathcal{B} = 2.072$ , whereas random search achieved  $\mathcal{B} = 2.076$ . It is worth noting that the corresponding circuit is significantly more convoluted, though, involving 42 gates for the random search compared to just 8 gates for the solution provided by the PPO agent. This non-optimal CHSH score is partially due to the fact that our agent is trained with modest computing power and does not rely on a large neural network. Therefore, the agent cannot learn complex circuit patterns required to reach higher CHSH scores. Moreover, learning a sub-optimal policy has the additional negative effect of reducing the exploration in later episodes, which further reduces the chances to find highly non-trivial circuits leading to higher CHSH scores. A summary of the circuits found by the PPO agent and by random search for the different strategies is provided in Appendix B.

We now focus on the circuit depicted in Fig. 1. This circuit appears as a good candidate for implementing a photonic Bell test with homodyne measurements. It has been found by the PPO agent interacting with a circuit of  $N = 4$  modes initialized with two two-mode squeezers and is composed of only two additional beam splitters. The third and fourth modes are used to herald the state using threshold detectors. This photonic circuit yields a CHSH score of  $\mathcal{B} = 2.068$  with optimal squeezing parameters corresponding to 3.9 dB and  $8 \cdot 10^{-3}$  dB of squeezing, respectively. The heralding probability of the state is  $3 \cdot 10^{-6}$ . Considering squeezers generating pulses at the MHz rate, the proposed circuit can prepare about 300 states per second. Therefore, the statistics for a Bell test can be gathered in a realistic amount of time, e.g.  $10^6$  shots in an hour.

We further study the impact of photon loss and inefficient detectors on the two most important metrics of the circuit, namely the CHSH score and the heralding probability.

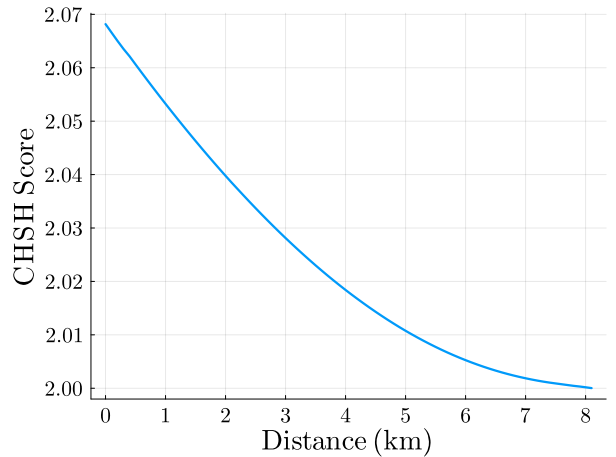


Figure 2: CHSH score with respect to the distance between Alice, where state preparation occurs, and Bob. We consider an optical fiber with a loss of 0.2 dB/km, and numerically optimized the circuits' parameters for each step of 0.1 km. As higher squeezing is beneficial for greater distance, we ensure squeezing of at most 10dB to respect practical experimental range.

To study the effect of photon loss, we assume that the optical circuit preparing and heralding the quantum state is located in Alice's laboratory. Bob receives his part of the state, i.e the second mode, through an optical fiber link characterized by 0.2 dB/km of attenuation. We assume that the optical signals are prepared at telecom wavelength, and, hence, that no conversion are necessary. In Fig. 2, we plot the CHSH score as a function of the distance between Alice and Bob. For every value of distance, we re-optimize the gates parameters to maximize the CHSH score. We observe that a CHSH violation is still possible for distances up to 8 km. As for the heralding probability of the state, this is not affected by photon loss occurring in Alice's or Bob's modes.

We then analyse the effect of imperfect detectors on circuit performance. Specifically, we assume that the threshold detectors used in the heralded modes have efficiency  $\eta < 1$ . In Fig. 3 we plot the heralding probability as a function of  $\eta$ , for fixed gate parameters optimal in the  $\eta = 1$  case. We observe that the heralding probability decreases by at most one order of magnitude for efficiencies  $\eta \geq 0.25$ . Moreover, we observe that the efficiency of the detectors has barely any impact on the CHSH score. Specifically, from a value  $\mathcal{B} = 2.068$  at  $\eta = 1.0$ , the CHSH score approaches  $\mathcal{B} = 2.067$  as  $\eta \rightarrow 0$ . This can be explained by the fact that the av-

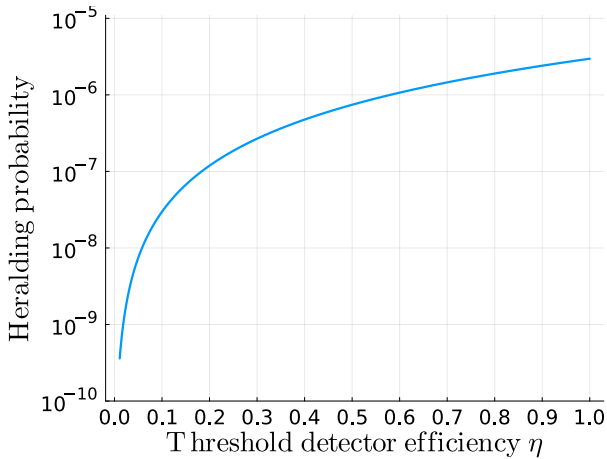


Figure 3: Evolution of the probability of a successful state heralding with respect to the efficiency of threshold detectors.

erage number of photons reaching the threshold detectors is well below 1. Indeed, if an inefficient threshold detector measures one mode out of a multi-photon entangled state, it detects each  $n$ -photon component of the state with a different probability,  $1 - (1 - \eta)^n$ , thereby modifying the photon number distribution of the unmeasured modes accordingly. This causes the conditional state of the unmeasured modes to depend, in principle, on the detector’s efficiency. However, if the multi-photon components in the measured mode are suppressed, the dependence of the conditional state on the detector efficiency becomes negligible, and the only real consequence is a reduction in the heralding probability.

Given the negligible impact of detector efficiency on the CHSH score and its minor influence on the heralding probability, we conclude that highly efficient detectors, such as single-photon detectors operating at cryogenic temperatures, are not required for a successful Bell tests using the proposed photonic circuit. Combined with its robustness to losses, this approach may enable loophole-free Bell tests using homodyne measurement and basic threshold detectors.

## 5 Conclusion

In this manuscript, we explore implementations for a photonic Bell inequality violation with homodyne measurements. We investigate practical optical setups, using standard optical components, with the aim of maximizing the violation of the CHSH inequality. This is achieved in an auto-

ated way thanks to reinforcement learning and random search, coupled with an efficient simulation framework of optical processes. By enforcing different sets of constraints on the explored photonic circuits, our approach leads to several circuits achieving a CHSH score higher than known proposals relying on homodyne measurements. In particular, a fairly simple circuit of four optical modes, two of which are heralded with threshold detectors, and four optical components reaches a CHSH score of 2.068. Through noise analysis, we have shown the resilience of the circuit against photon loss and its robustness to inefficient threshold detectors. The proposed circuit may open a way towards the first loophole-free Bell test with homodyne measurements. More broadly, the method described in this manuscript may be applied to discover photonic circuits using homodyne measurements, that could implement quantum information protocols relying on nonlocality, such as device-independent quantum key distribution.

## Acknowledgments

The authors acknowledge funding by the European Union’s Horizon Europe research and innovation program under the project “Quantum Security Networks Partnership” (QSNP, Grant Agreement No. 101114043) and by a French national quantum initiative managed by Agence Nationale de la Recherche in the framework of France 2030 with the reference ANR-22-PETQ-0009. FG did not contribute to this work on behalf of Leonardo S.p.A.

## References

- [1] John S Bell. “On the Einstein-Podolsky-Rosen paradox”. *Physics* **1**, 195–200 (1964). url: <http://cds.cern.ch/record/111654/files/>.
- [2] Nicolas Brunner, Daniel Cavalcanti, Stefano Pironio, Valerio Scarani, and Stephanie Wehner. “Bell nonlocality”. *Rev. Mod. Phys.* **86**, 419–478 (2014).
- [3] Rotem Arnon-Friedman. “Device-independent quantum information processing: A simplified analysis”. *Springer International Publishing*. (2020).



- [4] Xavier Valcarce. “Device-independent certification : quantum resources and quantum key distribution”. Theses. Université Paris-Saclay. (2023). url: <https://theses.hal.science/tel-04132704>.
- [5] Dominic Mayers and Andrew Yao. “Self testing quantum apparatus”. *Quantum Info. Comput.* **4**, 273–286 (2004).
- [6] Ivan Šupić and Joseph Bowles. “Self-testing of quantum systems: a review”. *Quantum* **4**, 337 (2020).
- [7] Antonio Acín, Nicolas Brunner, Nicolas Gisin, Serge Massar, Stefano Pironio, and Valerio Scarani. “Device-independent security of quantum cryptography against collective attacks”. *Physical Review Letters* **98** (2007).
- [8] Stefano Pironio, Antonio Acín, Nicolas Brunner, Nicolas Gisin, Serge Massar, and Valerio Scarani. “Device-independent quantum key distribution secure against collective attacks”. *New Journal of Physics* **11**, 045021 (2009).
- [9] Umesh Vazirani and Thomas Vidick. “Fully device-independent quantum key distribution”. *Physical Review Letters* **113** (2014).
- [10] Pavel Sekatski, Jean-Daniel Bancal, Xavier Valcarce, Ernest Y.-Z. Tan, Renato Renner, and Nicolas Sangouard. “Device-independent quantum key distribution from generalized CHSH inequalities”. *Quantum* **5**, 444 (2021).
- [11] Víctor Zapatero and Marcos Curty. “Long-distance device-independent quantum key distribution”. *Scientific Reports* **9** (2019).
- [12] René Schwonnek, Koon Tong Goh, Ignatius W. Primaatmaja, Ernest Y.-Z. Tan, Ramona Wolf, Valerio Scarani, and Charles C.-W. Lim. “Device-independent quantum key distribution with random key basis”. *Nature Communications* **12** (2021).
- [13] Víctor Zapatero, Tim van Leent, Rotem Arnon-Friedman, Wen-Zhao Liu, Qiang Zhang, Harald Weinfurter, and Marcos Curty. “Advances in device-independent quantum key distribution”. *npj Quantum Information* **9** (2023).
- [14] Antonio Acín and Lluís Masanes. “Certified randomness in quantum physics”. *Nature* **540**, 213–219 (2016).
- [15] John F. Clauser, Michael A. Horne, Abner Shimony, and Richard A. Holt. “Proposed experiment to test local hidden-variable theories”. *Phys. Rev. Lett.* **23**, 880–884 (1969).
- [16] B. Hensen, H. Bernien, A. E. Dréau, A. Reiserer, N. Kalb, M. S. Blok, J. Ruitenberg, R. F. L. Vermeulen, R. N. Schouten, C. Abellán, W. Amaya, V. Pruneri, M. W. Mitchell, M. Markham, D. J. Twitchen, D. Elkouss, S. Wehner, T. H. Taminiau, and R. Hanson. “Loophole-free bell inequality violation using electron spins separated by 1.3 kilometres”. *Nature* **526**, 682–686 (2015).
- [17] B. G. Christensen, K. T. McCusker, J. B. Altepeter, B. Calkins, T. Gerrits, A. E. Lita, A. Miller, L. K. Shalm, Y. Zhang, S. W. Nam, N. Brunner, C. C. W. Lim, N. Gisin, and P. G. Kwiat. “Detection-loophole-free test of quantum nonlocality, and applications”. *Phys. Rev. Lett.* **111**, 130406 (2013).
- [18] Lynden K. Shalm, Evan Meyer-Scott, Bradley G. Christensen, Peter Bierhorst, Michael A. Wayne, Martin J. Stevens, Thomas Gerrits, Scott Glancy, Deny R. Hamel, Michael S. Allman, Kevin J. Coakley, Shellee D. Dyer, Carson Hodge, Adriana E. Lita, Varun B. Verma, Camilla Lambrocco, Edward Tortorici, Alan L. Migdall, Yanbao Zhang, Daniel R. Kumar, William H. Farr, Francesco Marsili, Matthew D. Shaw, Jeffrey A. Stern, Carlos Abellán, Waldimar Amaya, Valerio Pruneri, Thomas Jennewein, Morgan W. Mitchell, Paul G. Kwiat, Joshua C. Bienfang, Richard P. Mirin, Emanuel Knill, and Sae Woo Nam. “Strong loophole-free test of local realism”. *Phys. Rev. Lett.* **115**, 250402 (2015).
- [19] Marissa Giustina, Marijn A. M. Versteegh, Sören Wengerowsky, Johannes Handsteiner, Armin Hochrainer, Kevin Phelan, Fabian Steinlechner, Johannes Kofler, Jan-Åke Larsson, Carlos Abellán, Waldimar Amaya, Valerio Pruneri, Morgan W. Mitchell, Jörn Beyer, Thomas Gerrits, Adriana E. Lita, Lynden K. Shalm, Sae Woo Nam, Thomas Scheidl, Rupert Ursin, Bernhard Wittmann, and Anton Zeilinger. “Significant-loophole-free test of bell’s theorem with entangled photons”. *Phys. Rev. Lett.* **115**, 250401 (2015).
- [20] Yang Liu, Qi Zhao, Ming-Han Li, Jian-

- Yu Guan, Yanbao Zhang, Bing Bai, Weijun Zhang, Wen-Zhao Liu, Cheng Wu, Xiao Yuan, Hao Li, W. J. Munro, Zhen Wang, Lixing You, Jun Zhang, Xiongfeng Ma, Jingyun Fan, Qiang Zhang, and Jian-Wei Pan. “Device-independent quantum random-number generation”. *Nature* **562**, 548–551 (2018).
- [21] Lijiong Shen, Jianwei Lee, Le Phuc Thinh, Jean-Daniel Bancal, Alessandro Cerè, Antia Lamas-Linares, Adriana Lita, Thomas Gerrits, Sae Woo Nam, Valerio Scarani, and Christian Kurtsiefer. “Randomness extraction from bell violation with continuous parametric down-conversion”. *Phys. Rev. Lett.* **121**, 150402 (2018).
- [22] Wenjamin Rosenfeld, Daniel Burchardt, Robert Garthoff, Kai Redeker, Norbert Ortengel, Markus Rau, and Harald Weinfurter. “Event-ready bell test using entangled atoms simultaneously closing detection and locality loopholes”. *Phys. Rev. Lett.* **119**, 010402 (2017).
- [23] Simon Storz, Josua Schär, Anatoly Kulikov, Paul Magnard, Philipp Kurpiers, Janis Lütolf, Theo Walter, Adrian Copetudo, Kevin Reuer, Abdulkadir Akin, Jean-Claude Besse, Mihai Gabureac, Graham J. Norris, Andrés Rosario, Ferran Martin, José Martinez, Waldimar Amaya, Morgan W. Mitchell, Carlos Abellan, Jean-Daniel Bancal, Nicolas Sangouard, Baptiste Royer, Alexandre Blais, and Andreas Wallraff. “Loophole-free bell inequality violation with superconducting circuits”. *Nature* **617**, 265–270 (2023).
- [24] D. P. Nadlinger, P. Drmota, B. C. Nichol, G. Araneda, D. Main, R. Srinivas, D. M. Lucas, C. J. Ballance, K. Ivanov, E. Y.-Z. Tan, P. Sekatski, R. L. Urbanke, R. Renner, N. Sangouard, and J.-D. Bancal. “Experimental quantum key distribution certified by bell’s theorem”. *Nature* **607**, 682–686 (2022).
- [25] Wei Zhang, Tim van Leent, Kai Redeker, Robert Garthoff, René Schwonnek, Florian Fertig, Sebastian Eppelt, Wenjamin Rosenfeld, Valerio Scarani, Charles C.-W. Lim, and Harald Weinfurter. “A device-independent quantum key distribution system for distant users”. *Nature* **607**, 687–691 (2022).
- [26] Wen-Zhao Liu, Yu-Zhe Zhang, Yi-Zheng Zhen, Ming-Han Li, Yang Liu, Jingyun Fan, Feihu Xu, Qiang Zhang, and Jian-Wei Pan. “Toward a photonic demonstration of device-independent quantum key distribution”. *Phys. Rev. Lett.* **129**, 050502 (2022).
- [27] A. Gilchrist, P. Deuar, and M. D. Reid. “Contradiction of quantum mechanics with local hidden variables for quadrature phase measurements on pair-coherent states and squeezed macroscopic superpositions of coherent states”. *Phys. Rev. A* **60**, 4259–4271 (1999).
- [28] W. J. Munro. “Optimal states for bell-inequality violations using quadrature-phase homodyne measurements”. *Phys. Rev. A* **59**, 4197–4201 (1999).
- [29] Jérôme Wenger, Mohammad Hafezi, Frédéric Grosshans, Rosa Tualle-Brouri, and Philippe Grangier. “Maximal violation of bell inequalities using continuous-variable measurements”. *Phys. Rev. A* **67**, 012105 (2003).
- [30] Enky Oudot, Gaël Massé, Xavier Valcarce, and Antonio Acín. “Realistic bell tests with homodyne measurements” (2024). [arXiv:2402.01530](https://arxiv.org/abs/2402.01530).
- [31] R. García-Patrón, J. Fiurášek, N. J. Cerf, J. Wenger, R. Tualle-Brouri, and Ph. Grangier. “Proposal for a loophole-free bell test using homodyne detection”. *Phys. Rev. Lett.* **93**, 130409 (2004).
- [32] Raúl García-Patrón, Jaromír Fiurášek, and Nicolas J. Cerf. “Loophole-free test of quantum nonlocality using high-efficiency homodyne detectors”. *Phys. Rev. A* **71**, 022105 (2005).
- [33] Jędrzej Kaniewski. “Analytic and nearly optimal self-testing bounds for the clauser-horne-shimony-holt and mermin inequalities”. *Physical Review Letters* **117** (2016).
- [34] Xavier Valcarce, Pavel Sekatski, Davide Orsucci, Enky Oudot, Jean-Daniel Bancal, and Nicolas Sangouard. “What is the minimum chsh score certifying that a state resembles the singlet?”. *Quantum* **4**, 246 (2020).
- [35] S. Tanzilli, A. Martin, F. Kaiser, M.P. De Micheli, O. Alibart, and D.B. Ostrowsky. “On the genesis and evolution of integrated quantum optics”. *Laser & Photonics Reviews* **6**, 115–143 (2012).
- [36] Emanuele Pelucchi, Giorgos Fagas, Igor

- Aharonovich, Dirk Englund, Eden Figueroa, Qihuang Gong, Hübel Hannes, Jin Liu, Chao-Yang Lu, Nobuyuki Matsuda, Jian-Wei Pan, Florian Schreck, Fabio Sciarrino, Christine Silberhorn, Jianwei Wang, and Klaus D. Jöns. “The potential and global outlook of integrated photonics for quantum technologies”. *Nature Reviews Physics* **4**, 194–208 (2021).
- [37] Volodymyr Mnih, Koray Kavukcuoglu, David Silver, Andrei A. Rusu, Joel Veness, Marc G. Bellemare, Alex Graves, Martin Riedmiller, Andreas K. Fidjeland, Georg Ostrovski, Stig Petersen, Charles Beattie, Amir Sadik, Ioannis Antonoglou, Helen King, Dhharshan Kumaran, Daan Wierstra, Shane Legg, and Demis Hassabis. “Human-level control through deep reinforcement learning”. *Nature* **518**, 529–533 (2015).
- [38] Volodymyr Mnih, Adrià Puigdomènech Badia, Mehdi Mirza, Alex Graves, Tim Harley, Timothy P. Lillicrap, David Silver, and Koray Kavukcuoglu. “Asynchronous methods for deep reinforcement learning”. In Proceedings of the 33rd International Conference on International Conference on Machine Learning - Volume 48. *Page 1928–1937*. ICML’16. JMLR.org (2016).
- [39] Tuomas Haarnoja, Aurick Zhou, Kristian Hartikainen, George Tucker, Sehoon Ha, Jie Tan, Vikash Kumar, Henry Zhu, Abhishek Gupta, Pieter Abbeel, and Sergey Levine. “Soft actor-critic algorithms and applications” (2018).
- [40] John Schulman, Sergey Levine, Philipp Moritz, Michael I. Jordan, and Pieter Abbeel. “Trust region policy optimization” (2015).
- [41] John Schulman, Filip Wolski, Prafulla Dhariwal, Alec Radford, and Oleg Klimov. “Proximal policy optimization algorithms” (2017).
- [42] Giuseppe Carleo, Ignacio Cirac, Kyle Cranmer, Laurent Daudet, Maria Schuld, Naf-tali Tishby, Leslie Vogt-Maranto, and Lenka Zdeborová. “Machine learning and the physical sciences”. *Rev. Mod. Phys.* **91**, 045002 (2019).
- [43] Jacob Biamonte, Peter Wittek, Nicola Pancotti, Patrick Rebentrost, Nathan Wiebe, and Seth Lloyd. “Quantum machine learning”. *Nature* **549**, 195–202 (2017).
- [44] Vedran Dunjko and Hans J Briegel. “Machine learning & artificial intelligence in the quantum domain: a review of recent progress”. *Rep. Prog. Phys.* **81**, 074001 (2018).
- [45] Mario Krenn, Manuel Erhard, and Anton Zeilinger. “Computer-inspired quantum experiments”. *Nature Reviews Physics* **2**, 649–661 (2020).
- [46] Mario Krenn, Mehul Malik, Robert Fickler, Radek Lapkiewicz, and Anton Zeilinger. “Automated search for new quantum experiments”. *Physical Review Letters* **116** (2016).
- [47] Alexey A. Melnikov, Pavel Sekatski, and Nicolas Sangouard. “Setting up experimental bell tests with reinforcement learning”. *Phys. Rev. Lett.* **125**, 160401 (2020).
- [48] Mario Krenn, Jakob S. Kottmann, Nora Tischler, and Alán Aspuru-Guzik. “Conceptual understanding through efficient automated design of quantum optical experiments”. *Physical Review X* **11** (2021).
- [49] X. Valcarce, P. Sekatski, E. Gouzien, A. Melnikov, and N. Sangouard. “Automated design of quantum-optical experiments for device-independent quantum key distribution”. *Phys. Rev. A* **107**, 062607 (2023).
- [50] B. S. Tsirel’son. “Quantum analogues of the bell inequalities. the case of two spatially separated domains”. *Journal of Soviet Mathematics* **36**, 557–570 (1987).
- [51] J. S. BELL. “Epr correlations and epw distributions”. *Annals of the New York Academy of Sciences* **480**, 263–266 (1986).
- [52] Michael G. Jabbour and Jonatan Bohr Brask. “Constructing local models for general measurements on bosonic gaussian states”. *Phys. Rev. Lett.* **131**, 110202 (2023).
- [53] A. Kuzmich, I. A. Walmsley, and L. Mandel. “Violation of bell’s inequality by a generalized einstein-podolsky-rosen state using homodyne detection”. *Phys. Rev. Lett.* **85**, 1349–1353 (2000).
- [54] Mattia Walschaers. “Non-gaussian quantum states and where to find them”. *PRX Quantum* **2**, 030204 (2021).
- [55] Xavier Valcarce. “Quantumopticalcircuits.jl”. <https://github.com/xvalcarce/QuantumOpticalCircuits.jl> (2021).

- [56] Jun Tian and other contributors. “Reinforcementlearning.jl: A reinforcement learning package for the julia programming language” (2020).
- [57] Werner Vogel and Dirk-Gunnar Welsch. “Quantum optics”. Wiley. (2006).
- [58] Stefano Pirandola, Alessio Serafini, and Seth Lloyd. “Correlation matrices of two-mode bosonic systems”. *Phys. Rev. A* **79**, 052327 (2009).

## A Photonic circuits

### A.1 Gaussian states

We consider circuits composed of  $N$  bosonic modes. Each mode is identified with an index  $i \in \{1, \dots, N\}$  and is associated with the ladder operators  $\hat{a}_i$  and  $\hat{a}_i^\dagger$  or, alternatively, to the dimensionless quadrature field operators  $\hat{x}_i = \frac{\hat{a}_i^\dagger + \hat{a}_i}{2}$  and  $\hat{p}_i = i\frac{\hat{a}_i^\dagger - \hat{a}_i}{2}$ , which satisfy the commutation relation:  $[\hat{x}_i, \hat{p}_i] = i\frac{1}{2}$ . By arranging the quadrature field operators in the vector:  $\hat{\mathbf{q}} = (\hat{x}_1, \hat{p}_1, \dots, \hat{x}_N, \hat{p}_N)$ , we have the commutation relation

$$[\hat{q}_k, \hat{q}_j] = i\frac{\Omega_{k,j}}{2}, \quad (12)$$

with  $\hat{q}_k$  the  $k$ -th component of the vector  $\hat{\mathbf{q}}$  and  $\Omega$  the symplectic matrix

$$\Omega = \bigoplus_{i=1}^N \omega, \quad \omega = \begin{pmatrix} 0 & 1 \\ -1 & 0 \end{pmatrix}. \quad (13)$$

The Wigner function of the state  $\rho$  of  $N$  bosonic modes is a quasi-probability distribution [57] defined as

$$W_\rho(\tilde{\alpha}) = \text{tr} \left( \hat{\rho} \bigotimes_{i=1}^N \delta(\hat{a}_i - \alpha_i) \right), \quad (14)$$

where  $\tilde{\alpha} \in \mathbb{R}^{2N}$  is the vector  $\tilde{\alpha} = \{\text{Re}(\alpha_1), \text{Im}(\alpha_1), \dots, \text{Re}(\alpha_n), \text{Im}(\alpha_n)\}^T$ , and

$$\delta(\hat{a} - \alpha) = \frac{1}{\pi^2} \int d^2\beta e^{i(\hat{a}^\dagger - \alpha^*)\beta - i(\hat{a} - \alpha)\beta^*}, \quad (15)$$

where  $d^2\beta = d\text{Re}(\beta) d\text{Im}(\beta)$ . A  $N$  bosonic modes quantum state can be expressed in terms of its Wigner function following

$$\hat{\rho} = \pi^N \int d^{2N}\tilde{\alpha} W(\tilde{\alpha}) \bigotimes_{i=1}^N \delta(\hat{a}_i - \alpha_i). \quad (16)$$

$\hat{\rho}$  is a Gaussian state if its Wigner function is equal to the probability density function of a multivariate normal distribution. That is, if it can be expressed in the form

$$W_{\mu, \Sigma}(\tilde{\alpha}) = \frac{\exp \left[ -\frac{1}{2}(\tilde{\alpha} - \boldsymbol{\mu})^T \Sigma^{-1}(\tilde{\alpha} - \boldsymbol{\mu}) \right]}{(2\pi)^n \sqrt{\det \Sigma}}, \quad (17)$$

where the displacement vector  $\boldsymbol{\mu}$  and the covariance matrix  $\Sigma$  have for elements

$$\mu_i = \langle \hat{q}_i \rangle, \quad (18)$$

$$\Sigma_{i,j} = \frac{1}{2} \langle \hat{q}_i \hat{q}_j + \hat{q}_j \hat{q}_i \rangle - \mu_i \mu_j. \quad (19)$$

Note that, due to the commutation relations in Eq. (12), an arbitrary real symmetric matrix  $\Sigma$  is a valid covariance matrix if and only if the inequality

$$\Sigma + i\frac{\Omega}{4} \geq 0. \quad (20)$$

is satisfied [58].

The total number of parameters for an  $N$ -mode Gaussian state consists of  $2N(2N + 1)$  elements from the upper triangular part of the covariance matrix  $\Sigma$  (accounting for its symmetry), along with  $2N$  elements from the displacement vector.

## A.2 Gaussian operations

Gaussian operations are particular unitary transformations  $\hat{U} = e^{i\hat{H}}$  which are generated by Hamiltonians  $\hat{H}$  that are linear and bilinear in the field modes. Such transformations are called Gaussian in that they preserve the Gaussian character of the state. As a matter of fact, the transformation induced on the quadrature operators preserves the commutation relations and reads

$$U^\dagger \hat{\mathbf{q}} U = M \hat{\mathbf{q}} + \mathbf{d}, \quad (21)$$

where  $\mathbf{d}$  is a real vector and  $M$  is a symplectic transformation, satisfying  $M\Omega M^T = \Omega$ , which characterize the Gaussian operation. Hence, given a Gaussian state with covariance matrix  $\Sigma$  and displacement vector  $\boldsymbol{\mu}$ , the resulting Gaussian state after applying a Gaussian operation  $(\mathbf{d}, M)$  is described by

$$\boldsymbol{\mu}' = M\boldsymbol{\mu} + \mathbf{d}, \quad (22)$$

$$\Sigma' = M\Sigma M^T. \quad (23)$$

In Table 1 we report the Gaussian operations, also named gates, that are considered in this manuscript, in terms of both the unitary transformation and the corresponding vector  $\mathbf{d}$  and symplectic matrix  $M$ . We adopt the notation for which the square brackets  $[i, j]$  indicate that the gate acts non-trivially on modes  $i$  and  $j$ , with  $i < j$ . Note that we restrict the parameters of each operation to the real domain, as any Gaussian operation with a complex parameter can be achieved with a combination of Gaussian operations with real parameters and phase shifters.

Importantly, Euler's decomposition ensures that every symplectic transformation  $M$  can be decomposed in the form

$$M = O \begin{pmatrix} D & 0 \\ 0 & D^{-1} \end{pmatrix} O', \quad (24)$$

where  $O$  and  $O'$  are orthogonal symplectic matrices and  $D$  is diagonal and positive definite. Physically, this implies that every Gaussian operation can be implemented by a sequence of passive beam-splitter and phase shifter gates (described by the orthogonal matrix  $O'$ ), followed by squeezer gates (matrix  $D$ ) and more passive gates (matrix  $O$ ). Moreover, if the initial Gaussian state is the vacuum – as is in our setup –, the first sequence of passive gates can be omitted since it acts trivially on the vacuum. Therefore, in our case, any Gaussian operation can be attained by an array of single mode squeezers, one per mode, followed by passive gates.

## A.3 Photon heralding

In this subsection, we review the conditional quantum state obtained by heralding the presence or absence of photons in a subset of its modes. The derivation of the formulas presented here can be found in [49].

Consider an  $N$ -mode Gaussian state  $\hat{\rho}$  with covariance matrix  $\Sigma$  and displacement vector  $\boldsymbol{\mu}$ . The quantum state  $\hat{\rho}_{-i} = \text{Tr}_i[\hat{\rho}]$  obtained by tracing out the  $i$ -th mode is still Gaussian, with displacement vector  $\boldsymbol{\mu}_{-i} = \text{TR}_i(\boldsymbol{\mu})$  and covariance matrix  $\Sigma_{-i} = \text{TR}_i(\Sigma)$ , where we defined  $\text{TR}_i(\cdot)$  as the operation that removes the rows and/or columns of a vector or matrix at positions  $2i - 1$  and  $2i$ .

Consider now the quantum state  $\hat{\rho}_{o_i}$  obtained from  $\hat{\rho}$  by measuring the  $i$ -th mode with a threshold detector, with efficiency  $\eta$ , and conditioning on a no-click event. By definition, the corresponding

Gaussian Operation	Unitary Operator	Symplectic Matrix
Phase Shifter	$\hat{R}(\theta)[i] = e^{-i\theta\hat{a}_i^\dagger\hat{a}_i}$	$M = \left( \begin{array}{c cc} \mathbb{I} & 0 & 0 \\ 0 & \cos(\theta) & \sin(\theta) \\ 0 & -\sin(\theta) & \cos(\theta) \\ \hline 0 & 0 & \mathbb{I} \end{array} \right)$
Single Mode Squeezer	$\hat{S}_1(r)[i] = e^{r[\hat{a}_i^2 - (\hat{a}_i^\dagger)^2]/2}$	$M = \left( \begin{array}{c cc} \mathbb{I} & 0 & 0 \\ 0 & e^{-r} & 0 \\ 0 & 0 & e^r \\ \hline 0 & 0 & \mathbb{I} \end{array} \right)$
Beam Splitter	$\hat{B}(\theta)[i, j] = e^{\theta(\hat{a}_i^\dagger\hat{a}_j - \hat{a}_i\hat{a}_j^\dagger)}$	$M = \left( \begin{array}{c ccc} \mathbb{I} & 0 & 0 & 0 \\ 0 & \cos(\theta)\mathbb{I}_2 & 0 & \sin(\theta)\mathbb{I}_2 \\ 0 & 0 & \mathbb{I} & 0 \\ 0 & -\sin(\theta)\mathbb{I}_2 & 0 & \cos(\theta)\mathbb{I}_2 \\ \hline 0 & 0 & 0 & \mathbb{I} \end{array} \right)$
Two Modes Squeezer	$\hat{S}_2(r)[i, j] = e^{r(\hat{a}_i\hat{a}_j - \hat{a}_i^\dagger\hat{a}_j^\dagger)}$	$M = \left( \begin{array}{c ccc} \mathbb{I} & 0 & 0 & 0 \\ 0 & \cosh(r)\mathbb{I}_2 & 0 & -\sinh(r)\mathbb{I}_2 \\ 0 & 0 & \mathbb{I} & 0 \\ 0 & -\sinh(r)\mathbb{I}_2 & 0 & \cosh(r)\mathbb{I}_2 \\ \hline 0 & 0 & 0 & \mathbb{I} \end{array} \right)$

Table 1: The Gaussian operations considered in this manuscript, when acting on an  $N$ -mode Gaussian state. Here  $\mathbb{I}_n$  is the  $n \times n$  identity matrix and  $\sigma_z$  is the third Pauli matrix. Note that the non-trivial  $2 \times 2$  blocks in the symplectic matrices correspond to the modes  $i$  and  $j$ , i.e. to rows/columns pairs  $2i - 1, 2i$  and  $2j - 1, 2j$ . For all the operations considered,  $\mathbf{d} = 0$ .

unnormalized state is  $p_{oi}\hat{\rho}_{oi} = \text{Tr}_i[(1 - \eta)^{\hat{a}_i^\dagger\hat{a}_i}\hat{\rho}]$ . One can show that the conditional state  $\hat{\rho}_{oi}$  is still Gaussian, with displacement vector and covariance matrix given by, respectively,

$$\begin{aligned} \boldsymbol{\mu}_{oi} &= \text{TR}_i[(\Sigma^{-1} + F)^{-1}\Sigma^{-1}\boldsymbol{\mu}] \\ \Sigma_{oi} &= \text{TR}_i[(\Sigma^{-1} + F)^{-1}], \end{aligned} \quad (25)$$

where the  $2N \times 2N$  matrix  $F$  is null everywhere except for the elements at position  $2i - 1$  and  $2i$ , which we write

$$F = \frac{4\eta}{2 - \eta} \left( \begin{array}{c|cc} 0 & 0 & 0 \\ 0 & \mathbb{I}_2 & 0 \\ 0 & 0 & 0 \end{array} \right). \quad (26)$$

Moreover, the probability of the no-click event is given by

$$p_{oi} = \frac{2}{2 - \eta} \sqrt{\frac{(\det \Sigma)^{-1}}{\det(\Sigma^{-1} + F)}} e^{-\frac{1}{2}\boldsymbol{\mu}^T[\Sigma^{-1} - \Sigma^{-1}(\Sigma^{-1} + F)^{-1}\Sigma^{-1}]\boldsymbol{\mu}}. \quad (27)$$

Consider now the quantum state  $\hat{\rho}_{\bullet i}$  obtained from  $\hat{\rho}$  by measuring the  $i$ -th mode with a threshold detector, with efficiency  $\eta$ , and conditioning on a click event. By definition, the corresponding unnormalized state is  $p_{\bullet i}\hat{\rho}_{\bullet i} = \text{Tr}_i[(\mathbb{I} - (1 - \eta)^{\hat{a}_i^\dagger\hat{a}_i})\hat{\rho}]$ . We deduce that  $\hat{\rho}_{\bullet i}$  is a linear combination of two Gaussian states with a negative coefficient

$$\hat{\rho}_{\bullet i} = \frac{1}{p_{\bullet i}}\hat{\rho}_{-i} - \frac{p_{oi}}{p_{\bullet i}}\hat{\rho}_{oi}, \quad (28)$$

where the heralding probability is  $p_{\bullet i} = 1 - p_{oi}$ , with  $p_{oi}$  defined in Eq. (27).

#### A.4 CHSH score from homodyne measurements

In order to numerically compute the correlators  $\langle A_x B_y \rangle$  appearing in the CHSH score, we start by expressing the joint probability of Alice's and Bob's quadrature outcomes as a linear combination of Gaussian distributions. In the following, we omit the explicit indication of Alice's and Bob's measurement inputs for ease of notation. We obtain

$$P(x_1, x_2) = \iint_{-\infty}^{\infty} dp_1 dp_2 \tilde{W}_{12}(x_1, p_1, x_2, p_2) \quad (29)$$

$$= \sum_k w_k \iint_{-\infty}^{\infty} dp_1 dp_2 W_{12}^k(x_1, p_1, x_2, p_2) \quad (30)$$

$$= \sum_k w_k \frac{\exp\left[-\frac{1}{2}(\tilde{\alpha} - \mu_k)^T \sigma_k^{-1} (\tilde{\alpha} - \mu_k)\right]}{2\pi\sqrt{\det \sigma_k}}, \quad (31)$$

where in the first equality we express the Wigner function of the heralded state as a linear combination of Gaussian Wigner functions,  $W_{12}^k$ , according to Eq. (10), while in the second equality we compute the marginal of a Gaussian distribution. In particular, the  $2 \times 2$  matrix  $\sigma_k$  is obtained from the covariance matrix of the  $k$ -th Gaussian state by removing the second and fourth row and column, while the 2-dimensional vector  $\mu_k$  is obtained from the first and third entry of the displacement vector of the  $k$ -th Gaussian state. Finally, we have that  $\tilde{\alpha}^T = (x_1, x_2)$ .

Although the matrices  $\sigma_k$  are symmetric and satisfy  $\sigma_k \geq 0$ , the exponential functions in Eq. (31) are not necessarily Gaussian. This is because integrating a Gaussian Wigner function over the variables  $p_1$  and  $p_2$  does not always result in a Gaussian distribution. In particular, if the matrices  $\sigma_k$  are singular, the expression becomes undefined. However, in practice, the determinants are never exactly zero, allowing us to safely use the expression in Eq. (31).

Now, let us consider a general binning function  $a(x_1) : \mathbb{R} \rightarrow \{-1, 1\}$  for Alice and  $b(x_2) : \mathbb{R} \rightarrow \{-1, 1\}$  for Bob. The special case of sign binning is recovered for  $a(x) = b(x) = 1$  for  $x > 0$  and  $a(x) = b(x) = -1$  otherwise. Then, the generic correlator appearing in the CHSH score is expressed in terms of the joint probability  $P(x_1, x_2)$  as

$$\langle A_x B_y \rangle = \iint_{-\infty}^{\infty} dx_1 dx_2 a(x_1) b(x_2) P(x_1, x_2). \quad (32)$$

By employing the result in Eq. (31), we can recast the above expression as

$$\begin{aligned} \langle A_x B_y \rangle = \sum_k w_k \left[ \iint_{R_+} dx_1 dx_2 \frac{\exp\left[-\frac{1}{2}(\tilde{\alpha} - \mu_k)^T \sigma_k^{-1} (\tilde{\alpha} - \mu_k)\right]}{2\pi\sqrt{\det \sigma_k}} \right. \\ \left. - \iint_{R_-} dx_1 dx_2 \frac{\exp\left[-\frac{1}{2}(\tilde{\alpha} - \mu_k)^T \sigma_k^{-1} (\tilde{\alpha} - \mu_k)\right]}{2\pi\sqrt{\det \sigma_k}} \right], \end{aligned} \quad (33)$$

where we defined regions  $R_{\pm}$ ,  $R_{\pm} = \{(x_1, x_2) : a(x_1) = \pm b(x_2)\}$ , such that  $\mathbb{R}^2 = R_+ \cup R_-$ . Considering that the integrand function is normalized to one and that  $\sum_k w_k = 1$ , we can write

$$\langle A_x B_y \rangle = -1 + 2 \sum_k w_k \iint_{R_+} dx_1 dx_2 \frac{\exp\left[-\frac{1}{2}(\tilde{\alpha} - \mu_k)^T \sigma_k^{-1} (\tilde{\alpha} - \mu_k)\right]}{2\pi\sqrt{\det \sigma_k}}. \quad (34)$$

Note that the region  $R_+$  is given by a set of disjoint rectangular areas  $R_{\square} = [u_1, v_1] \times [u_2, v_2]$  that depend on the specific choice of binning functions  $a(x)$  and  $b(x)$ . Thus, for the sake of calculating Eq. (34), we are interested in the integral

$$I = \int_{u_1}^{v_1} dx_1 \int_{u_2}^{v_2} dx_2 \exp\left[-\frac{1}{2}\tilde{\alpha}^T A \tilde{\alpha}\right], \quad (35)$$

where  $A$  is a symmetric positive semi-definite matrix

$$A = \begin{pmatrix} r & t \\ t & s \end{pmatrix}. \quad (36)$$

By partially integrating over  $x_1$ , one can show that the integral in Eq. (35) reduces to

$$I = \int_{\frac{u_2}{\sqrt{2}}}^{\frac{v_2}{\sqrt{2}}} dx_2 e^{-x_2^2 \frac{rs-t^2}{r}} \sqrt{\frac{\pi}{r}} \left[ \text{Erf} \left( \sqrt{\frac{r}{2}} v_1 + \frac{t}{\sqrt{r}} x_2 \right) - \text{Erf} \left( \sqrt{\frac{r}{2}} u_1 + \frac{t}{\sqrt{r}} x_2 \right) \right], \quad (37)$$

where we introduced the error function

$$\text{Erf}(z) = \frac{2}{\sqrt{\pi}} \int_0^z dt e^{-t^2}. \quad (38)$$

We recast the correlator in Eq. (34) as

$$\langle A_x B_y \rangle = -1 + 2 \sum_k w_k \sum_{R_\square \in R_+} I_\square, \quad (39)$$

where the quantities  $I_\square$  are obtained via Eq. (37) and read

$$I_\square = \int_{u_1}^{v_1} dx_1 \int_{u_2}^{v_2} dx_2 \frac{\exp \left[ -\frac{1}{2} (\tilde{\alpha} - \boldsymbol{\mu}_k)^T \sigma_k^{-1} (\tilde{\alpha} - \boldsymbol{\mu}_k) \right]}{2\pi \sqrt{\det \sigma_k}} \quad (40)$$

$$= \frac{1}{2\sqrt{\pi}} \int_{\frac{u_2 - (\boldsymbol{\mu}_k)_2}{\sqrt{2\sigma_b}}}^{\frac{v_2 - (\boldsymbol{\mu}_k)_2}{\sqrt{2\sigma_b}}} dy e^{-y^2} \left[ \text{Erf} \left( \frac{\sqrt{\sigma_b} \frac{v_1 - (\boldsymbol{\mu}_k)_1}{\sqrt{2}} - \sigma_c y}{\sqrt{\det \sigma_k}} \right) - \text{Erf} \left( \frac{\sqrt{\sigma_b} \frac{u_1 - (\boldsymbol{\mu}_k)_1}{\sqrt{2}} - \sigma_c y}{\sqrt{\det \sigma_k}} \right) \right], \quad (41)$$

where we parametrized the matrix  $\sigma_k$  as

$$\sigma_k = \begin{pmatrix} \sigma_a & \sigma_c \\ \sigma_c & \sigma_b \end{pmatrix}. \quad (42)$$

One can then employ Eq. (39), in combination with a numerical computation of Eq. (41), to compute the CHSH score for any arbitrary choice of binning functions. For the specific choice that we made in our work, i.e. sign binning, we have

$$\langle A_x B_y \rangle = -1 + 2 \sum_k w_k (I_k + I'_k), \quad (43)$$

where  $I_k$  and  $I'_k$  are obtained by numerically solving Eq. (41) with parameters  $u_1 = u_2 = 0$  and  $v_1 = v_2 = \infty$  for  $I_k$  and  $u_1 = u_2 = -\infty$  and  $v_1 = v_2 = 0$  for  $I'_k$ .

## B Automated generation of photonic Bell tests

### B.1 Exploring photonic setups

We explore  $N$ -mode photonic circuits composed of  $n_{\text{circuit}}$  optical elements. Photonic operations are applied to the  $N$ -modes during a state preparation phase. The last  $N - 2$  modes are then heralded, while the first two modes are sent to Alice and Bob respectively.

To enhance the experimental relevance of discovered circuit and the chance to find interesting setups, we devise exploration strategies; constraints on the initial state and on the type of the available photonic operations. The strategies are detailed in Table 2. These strategies are physically-informed, they leverage knowledge on photonic state construction and answer practical experimental requirements.



Strategy	Initial state	Photonic operations
1	Vacuum state	$S_1, S_2, R, B$
2	$S_2$ gate on mode 1,2	Passive gates ( $R, B$ )
3	$S_2$ gate every pair of modes (1,2 / 3,4 / ..)	Passive gates ( $R, B$ )
4	$S_1$ gate on mode 1 and 2	Passive gates ( $R, B$ )
5	$S_1$ gate on every mode	Passive gates ( $R, B$ )

Table 2: Circuit exploration strategies. A strategy is characterized by a fixed initial state construction followed by specific photonic operations.  $S_1$  and  $S_2$  label single- and two-mode squeezer,  $R$  is phase-shifter, and  $B$  represents beam-splitter.

We remark that all strategies but Strategy 1 are characterized by having the initial vacuum modes initialized by active gates  $S_1$  and  $S_2$ , followed by only passive gates. This approach has some advantages. First of all, by virtue of Euler’s decomposition in Eq. (24), this approach is non-restrictive as it still enables us to explore the whole set of circuits that can be generated by the full set of gates. Second, we avoid circuits with multiple squeezers in sequence, which not only may be experimentally challenging but can also cause numerical errors due to a compounded large squeezing parameter, thereby invalidating the results.

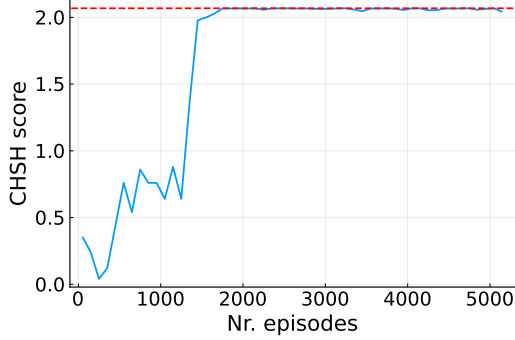
For each strategy, we explored two heralding mechanisms. In Fig. 4 we schematize these two mechanisms on a single mode. One possibility is to herald the state on a click in a single threshold detector, as depicted in Fig. 4(a) (c.f. Eq. (28) in Appendix A). Alternatively, we approximate the measurement that projects on a single photon, namely the POVM  $\{|1\rangle\langle 1|, \mathbb{I} - |1\rangle\langle 1|\}$ , where  $|1\rangle$  is a Fock state, with the setup depicted in Fig. 4(b). We achieve this by mixing the mode with the vacuum through an unbalanced beam splitter,  $\hat{B}(0.1)$ . We then herald the state on a click in the reflected port and a no-click, c.f. Eq. (25), in the transmitted port. By doing so, the heralding event occurs with low probability since most of the time the photons in the measured mode are transmitted and the event discarded. However, when we have a successful heralding, there is a high probability that the click in the reflected port was caused by exactly one photon due to the low reflectivity of the beam splitter, and at the same time the no-click in the transmitted port guarantees that no other photon was detected. Overall, this simulates a good approximation of the projection on a single photon, provided that the detectors involved are ideal.

## B.2 Results

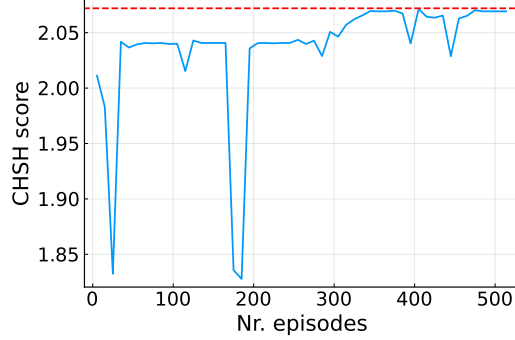
We run the random search and reinforcement learning routine over a fixed number of episodes, where each episode terminates when the circuit depth reaches its maximum predefined value,  $n_{\text{circuit}}$ . We



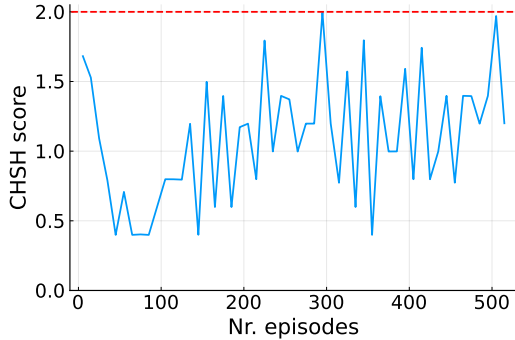
Figure 4: Two alternative ways to herald a mode. In (a), we herald the state on a click in a threshold detector. In (b), we approximate a projection on a single photon by mixing the mode with the vacuum through a beam-splitter with parameter  $\theta = 0.1$  (the transmittance of the beam-splitter is  $\cos(0.1) \approx 0.995$ ). Then, we herald on a click in the threshold detector at the reflected port and a no-click in the transmitted port. This combined event heralds on the detection of a single photon with high probability.



(a) Strategy 1,  $N = 4$  modes,  $n_{\text{circuit}} = 4$  total gates, heralding scheme: single-photon projection.



(b) Strategy 3,  $N = 6$  modes,  $n_{\text{circuit}} = 12$  total gates, heralding scheme: single-photon projection.



(c) Strategy 5,  $N = 6$  modes,  $n_{\text{circuit}} = 20$  total gates, heralding scheme: single-photon projection.

Figure 5: The evolution of the CHSH score with the number of completed episodes, for an agent with PPO policy implementing three different strategies to build the optical circuits (c.f. Appendix B). In both (a) and (b), the increase of the CHSH score with the number of episodes shows that the agent learns from previous interactions with the environment to produce circuits with higher CHSH violations. In particular, the agent finds circuits with CHSH score equal to 2.068 (red dashed line) in (a) and 2.072 (red dashed line) in (b). Conversely, the CHSH score remains constantly below 2.0 (red line) in (c), signifying that the agent could not learn a policy leading to CHSH violations. Samples of the circuits found with the three strategies are reported in Table 4.

explored different values of  $n_{\text{circuit}}$  to verify what violations can be achieved both in circuits with few gates and in circuits with large depth. The photonic gates parameters are optimized at the end of each episode such that the CHSH score is maximized, with a numerical procedure based on Nelder-Mead optimization. Subsequently, we fix the CHSH score and optimize the gates parameters to maximize the total heralding probability of the state.

In Table 3 and Table 4, we report a selection of photonic circuits found by random search and reinforcement learning, characterized by their CHSH score and heralding probability. We focus on circuits with  $N = 4$  and  $N = 6$  modes, as our findings suggest that five modes offer no significant advantage over four.

In order to evaluate the various strategies without having to fine tune the RL parameters (e.g. update frequency, trajectory capacity, clip range, ADAM optimizer, and so on), we perform a random search, where the photonic operations are selected uniformly at random in each step, thereby saving us some time. In this evaluation, strategies 2 and 4 appear suboptimal (c.f. Table 3), and we thus focus on the other strategies.

The circuits found by the agent in Table 4 are representative of the learning process occurring with the PPO policy. In fact, Table 4 reports circuits found by the agent towards the end of the training process, where the CHSH score associated with the circuit becomes larger. The learning process can

be visualized with the plots in Fig. 5, which show the progression of the CHSH score over the training episodes. We observe that, for Strategy 1 in Fig. 5(a) and Strategy 3 in Fig. 5(b), the CHSH score improves over the training and reaches the maximum value in the later episodes. Conversely, it seems that the PPO agent struggles to learn circuit patterns leading to CHSH violations when adopting Strategy 5. This could be explained by the fact that, in Strategy 5, Alice’s and Bob’s modes are initialized in a product state that would result, if measured, in uncorrelated measurement outcomes ( $\langle A_x B_y \rangle = 0$ ), opposed to the correlations that arise when initializing the modes with a two-mode squeezer ( $\langle A_x B_y \rangle > 0$ ). This means that the starting value of the CHSH score, when the circuit is still empty, with Strategy 5 is closer to zero compared to Strategy 3, where it starts closer to 2. Thus, it is easier for the agent in Strategy 3 to find circuit patterns leading to CHSH violations than when Strategy 5 is adopted. Still, we observe that the PPO agent in Strategy 5 can find circuits leading to a CHSH score of 2.0, i.e., a policy that generate (trivial) classical correlations between Alice and Bob is learned.

Finally, training the agent both with the PPO policy and the random search allows us to benchmark the usefulness of a learning agent for circuit generation. By comparing the circuits found in Tables 3 and 4, there is no apparent advantage in using a trained agent to find good candidate circuits, compared to a random search, in this scenario. We remark, however, that this conclusion holds in the context of our RL trainings, which are limited by the computational power of a personal computer and by a shallow neural network with two hidden layers, but we expect a larger neural network to perform better than the one used here. Furthermore, we expect the performance of an unstructured search to be less appealing when trying to construct circuits in larger scenarios, e.g. involving more than two parties.

Table 3: Circuits found by the agent with random search. “S.” indicates the strategy adopted,  $g$  is the number of Gaussian operations, where we indicate in brackets the number of active Gaussian operations (squeezers). The notation is the one adopted in Table 1 and the gates are applied sequentially in the same order as they appear in the list. We omit the  $\hat{\cdot}$  symbol in the gates list for ease of notation. The heralding of the modes  $3, 4, \dots, N$  is “cl.” when the state is heralded on a click in a threshold detector, and “s.p.” when attained by simulating a single photon projection; we also report the total heralding probability of the state under “Herald.”.

S.	$N$	$g$	Gates	Herald.	CHSH
1	4	4(2)	$S_2(0.44628)[1, 2]$ $B(1.60873)[1, 3]$ $S_2(0.03308)[3, 4]$ $B(1.60953)[1, 3]$	cl. $5.0 \cdot 10^{-6}$	2.068
		4	$S_2(0.4455)[1, 4]$ $B(3.06797)[1, 3]$ $B(1.61219)[2, 4]$ $S_2(0.01711)[1, 4]$	cl. $4.9 \cdot 10^{-6}$	2.068
2	4	6(1)	$S_2(1.51498)[1, 2]$ $B(1.38042)[1, 4]$ $B(1.79175)[1, 2]$ $B(3.54325)[1, 3]$ $B(0.92456)[1, 4]$ $B(2.50137)[2, 4]$	s.p. $4.7 \cdot 10^{-6}$	2.060
		3	$S_2(0.00095)[1, 2]$ $S_2(0.4501)[3, 4]$ $B(1.50217)[2, 4]$ $R(0.47822)[4]$ $B(1.63927)[1, 3]$	cl. $3.2 \cdot 10^{-6}$	2.068
4	8(2)	$S_2(0.00102)[1, 2]$ $S_2(0.44752)[3, 4]$ $B(1.62564)[1, 2]$ $B(1.49052)[2, 3]$ $B(1.31128)[1, 2]$ $B(1.63383)[2, 4]$ $R(2.10579)[3]$ $B(2.88315)[1, 4]$	cl. $3.3 \cdot 10^{-6}$	2.068	
		4	$S_2(0.45013)[1, 2]$ $S_2(0.00127)[3, 4]$ $B(2.83692)[3, 4]$ $B(2.21531)[1, 4]$ $B(1.68516)[1, 2]$ $B(1.47966)[3, 4]$ $B(1.83057)[1, 2]$ $B(1.30233)[2, 3]$ $B(2.16635)[1, 2]$ $R(0.21311)[4]$ $B(1.03997)[2, 3]$	cl. $4.1 \cdot 10^{-6}$	2.068
6	9(3)	$S_2(0.4886)[1, 2]$ $S_2(0.0103)[3, 4]$ $S_2(1.14363)[5, 6]$ $B(1.93776)[2, 6]$ $R(0.40101)[3]$ $B(1.56028)[5, 6]$ $B(2.65334)[4, 5]$ $B(2.1377)[3, 6]$ $B(1.79887)[1, 3]$	s.p. $1.8 \cdot 10^{-11}$	2.073	
		4	$S_1(1.57601)[1]$ $S_1(0.30398)[2]$ $R(1.57557)[2]$ $B(1.38422)[1, 3]$ $B(1.44189)[1, 4]$ $B(0.20825)[2, 3]$ $B(1.75776)[3, 4]$ $B(1.54447)[1, 4]$ $B(2.75608)[1, 2]$	cl. $1.2 \cdot 10^{-8}$	2.063
5	4	17(4)	$S_1(1.37645)[1]$ $S_1(0.00168)[2]$ $S_1(0.00599)[3]$ $S_1(0.22444)[4]$ $R(0.00749)[3]$ $B(0.58858)[1, 2]$ $R(0.54082)[4]$ $B(3.14062)[2, 3]$ $B(2.69734)[1, 3]$ $B(2.30103)[1, 2]$ $B(1.56934)[3, 4]$ $R(1.02956)[3]$ $B(0.94574)[1, 4]$ $B(4.25384)[1, 3]$ $B(1.31202)[2, 3]$ $B(1.74175)[1, 2]$ $B(2.5986)[1, 4]$	cl. $1.2 \cdot 10^{-5}$	2.066
		4	$S_1(0.70577)[1]$ $S_1(0.00066)[2]$ $S_1(0.4052)[3]$ $S_1(0.06303)[4]$ $B(1.29941)[2, 3]$ $B(1.4099)[1, 3]$ $B(1.02284)[2, 3]$ $R(0.91296)[1]$ $R(0.95323)[3]$ $R(1.44978)[3]$ $B(1.97387)[1, 3]$ $B(2.60931)[2, 4]$ $R(0.43968)[4]$ $B(1.37219)[1, 2]$ $R(0.62318)[3]$ $B(2.97856)[1, 3]$ $B(2.17853)[1, 2]$	s.p. $2.1 \cdot 10^{-7}$	2.068
4	11(4)	$S_1(1.99879)[1]$ $S_1(0.27027)[2]$ $S_1(0.02467)[3]$ $S_1(0.14767)[4]$ $B(1.5709)[1, 2]$ $R(1.57177)[1]$ $B(1.19975)[1, 3]$ $B(2.85582)[2, 3]$ $B(1.94903)[3, 4]$ $B(1.62179)[1, 4]$ $B(1.71619)[1, 2]$	s.p. $2.3 \cdot 10^{-7}$	2.068	

(Continued on next page ...)

Table 3 – Continued from previous page

S.	$N$	$g$	Gates	Herald.	CHSH
6	27(6)		$S_1(0.13442)[1]$ $S_1(0.01894)[2]$ $S_1(0.23412)[3]$ $S_1(0.75517)[4]$ $S_1(1.91139)[5]$ $S_1(0.06771)[6]$ $B(0.77041)[1, 4]$ $B(1.44169)[1, 2]$ $B(0.84147)[1, 4]$ $R(0.33784)[4]$ $B(1.05774)[5, 6]$ $B(1.41175)[2, 5]$ $B(1.0452)[2, 4]$ $B(1.83876)[2, 6]$ $B(1.59497)[1, 3]$ $R(1.52075)[4]$ $B(0.77169)[1, 2]$ $R(0.69784)[2]$ $B(1.34197)[1, 3]$ $B(1.67829)[1, 4]$ $B(2.63474)[2, 3]$ $R(1.42985)[2]$ $B(1.90975)[3, 5]$ $B(2.04856)[4, 5]$ $R(2.17427)[5]$ $B(2.3683)[2, 3]$ $B(0.98299)[1, 4]$	s.p. $3.5 \cdot 10^{-12}$	2.070
6	42(6)		$S_1(1.33522)[1]$ $S_1(0.50981)[2]$ $S_1(1.35176)[3]$ $S_1(1.78416)[4]$ $S_1(1.56906)[5]$ $S_1(0.14952)[6]$ $B(1.45766)[2, 3]$ $B(1.12)[2, 5]$ $B(1.13792)[3, 6]$ $R(1.21553)[6]$ $B(1.61669)[4, 6]$ $R(0.52559)[2]$ $B(1.40038)[3, 6]$ $B(1.89262)[2, 6]$ $B(1.80117)[4, 5]$ $R(0.58755)[6]$ $B(2.19939)[1, 5]$ $B(1.41454)[4, 6]$ $B(2.14052)[3, 5]$ $R(0.49489)[2]$ $B(1.97156)[5, 6]$ $R(0.42675)[1]$ $B(2.04066)[2, 5]$ $B(1.88537)[3, 6]$ $B(2.04211)[2, 5]$ $B(1.75719)[4, 5]$ $B(1.39104)[1, 2]$ $B(1.84995)[2, 6]$ $B(1.24971)[5, 6]$ $R(0.5619)[6]$ $B(1.20624)[2, 3]$ $R(0.17554)[5]$ $B(1.29781)[2, 3]$ $R(0.98721)[2]$ $R(0.30125)[1]$ $B(1.76338)[1, 2]$ $B(1.66911)[3, 6]$ $B(1.26734)[1, 5]$ $R(0.35314)[4]$ $B(1.47)[1, 4]$ $B(1.25175)[1, 3]$ $R(1.80732)[4]$	s.p. $1.7 \cdot 10^{-11}$	2.076

Table 4: Circuits found using reinforcement learning with the PPO policy. The same notation of Table 3 applies.

S.	$N$	$g$	Gates	Herald.	CHSH
1	4	4(3)	$S_2(0.58994)[1, 2]$ $S_2(1.13938)[3, 4]$ $B(2.83528)[2, 4]$ $S_2(1.15427)[3, 4]$	s.p. $3.0 \cdot 10^{-6}$	2.068
1	4	4(2)	$S_2(0.00462)[3, 4]$ $B(1.62748)[2, 4]$ $S_2(0.44529)[1, 2]$ $B(3.01595)[2, 4]$	s.p. $2.1 \cdot 10^{-11}$	2.069
3	4	4(2)	$S_2(0.00096)[1, 2]$ $S_2(0.44993)[3, 4]$ $B(1.63856)[2, 4]$ $B(1.50272)[1, 3]$	cl. $3.0 \cdot 10^{-6}$	2.068
3	6	8(3)	$S_2(1.00266)[1, 2]$ $S_2(0.77432)[3, 4]$ $S_2(0.05986)[5, 6]$ $B(3.1033)[4, 6]$ $B(2.90802)[2, 3]$ $B(1.13535)[4, 6]$ $B(2.84339)[2, 5]$ $B(0.38529)[2, 3]$	s.p. $1.1 \cdot 10^{-11}$	2.072
5	4	10(4)	$S_1(0.97488)[1]$ $S_1(0.03222)[2]$ $S_1(1.16719)[3]$ $R(1.56407)[1]$ $B(1.39216)[3, 4]$ $B(2.53958)[1, 4]$ $B(1.28743)[1, 2]$ $B(1.09283)[1, 4]$ $B(2.36714)[3, 4]$	s.p. $2.3 \cdot 10^{-6}$	2.030
5	6	20(6)	$S_1(1.8)[1]$ $S_1(1.8)[2]$ $S_1(1.0)[3]$ $S_1(1.0)[4]$ $S_1(1.0)[5]$ $S_1(1.0)[6]$ $R(1.57318)[1]$ $B(2.35548)[1, 2]$ $R(0)[1]$ $R(0)[1]$ $R(0)[1]$ $R(0)[1]$ $R(0)[1]$ $R(0)[1]$ $R(0)[1]$ $R(0)[1]$ $R(0)[1]$ $R(0)[1]$	s.p. $1.2 \cdot 10^{-19}$	1.996